Stellar collisions in young star clusters

Gaburov, E.

Publication date
2008

Chapter 7

The evolution of runaway stellar collision products

Based on:
E. Glebbeek, E. Gaburov, S. de Mink, O. Pols and S. Portegies Zwart
Astronomy & Astrophysics, submitted

ABSTRACT

In the cores of young dense star clusters repeated stellar collisions involving the same object can occur, which has been suggested to lead to the formation of an intermediate-mass black hole. In order to verify this scenario we compute the detailed evolution of the merger remnant of three sequences. We follow the evolution until the onset of carbon burning and estimate the final remnant mass to determine the ultimate fate of a runaway merger sequence.

We use a detailed stellar evolution code to follow the evolution of the collision product between collisions. At each collision, we mix the two colliding stars, taking account of mass loss from the collision. During the stellar evolution we apply mass loss rates from the literature, as appropriate for the evolutionary stage of the merger remnant. We compute models for high ($Z = 0.02$) and low ($Z = 0.001$) metallicity to quantify metallicity effects.

We find that the merger remnant becomes a Wolf-Rayet star before the end of core hydrogen burning. Mass loss from stellar winds dominates over the mass increase due to repeated mergers for all three merger sequences that we consider. In none of our high metallicity models an intermediate-mass black hole is formed, instead they end their lives as 10–14 $M_\odot$ black holes. For low metallicity we expect the final remnant of the merger sequence to explode as a pair creation supernova. We find that our metal-rich models become inflated as a result of developing an extended low-density envelope. This may increase the probability of further collisions, but self-consistent N-body calculations with detailed evolution of runaway mergers are required to verify this.

7.1 Introduction

The usual mode of star formation leads to a spectrum of masses between the theoretical hydrogen burning limit and some upper limit, which appears to be close to about $100\,M_\odot$ (Elmegreen, 1999; Weidner & Kroupa, 2004; Figer, 2005). In young and dense star clusters more massive stars can form when two or more high-mass stars coalesce. The cluster environment helps in driving these stars together. If this happens in sufficiently young and dense star cluster the same star may experience multiple collisions in what is named a 'collisional runaway' (Portegies Zwart et al., 1999). During such a chain collision several stars collide in short succession. The trigger for a chain collision is the gravothermal collapse (Bettwieser & Sugimoto, 1984) of the core of a young and dense star cluster. If cluster core collapse is initiated before the most massive stars leave the main sequence the collision runaway sets in (Portegies Zwart & McMillan, 2002) and continues until the target star leaves the main sequence (Portegies Zwart et al., 1999).

If the star explodes as a supernova, this supernova is likely to be unusually bright and rich in hydrogen (Portegies Zwart & van den Heuvel, 2007). The star may also collapse completely into a black hole, without a visible supernova. The black hole remnant of such a star may be considerably more massive than hitherto observed (Portegies Zwart et al., 2004), though less massive than the supermassive black holes found in the nuclei of large galaxies (Kormendy & Richstone, 1995). Various groups have now confirmed the evolution of such collision runaways, and conjecture that the final merger product collapses to a black hole of up to about $10^3\,M_\odot$ (Portegies Zwart et al., 1999, 2004; Freitag et al., 2006; Gürkan et al., 2006).

Two of our aims in understanding merger runaways are understanding the structure of the merger remnant and the influence of stellar evolution of the merger runaway. Stellar evolution of very massive stars (with masses above $150\,M_\odot$) has recently been studied by Belkus et al. (2007), Yungelson et al. (2008) and Langer et al. (2007). These studies all seem to come to the same conclusion: at high metallicity mass loss is copious enough to prevent the formation of a black hole of more than $50\,M_\odot$, which is much lower than the conjectured intermediate-mass black hole mass. These studies, however, either used approximate formulae for stellar evolution (Belkus et al., 2007) or studied the evolution of very massive stars from the zero-age main sequence with an initially homogeneous composition (Yungelson et al., 2008; Langer et al., 2007). According to the dynamical simulations the massive star grows in mass by means of repeated collisions with less massive stars. The consequences of the collisions, the evolution between collisions and the differences in stellar age and structure at the moment of collision are not considered by these studies. A first attempt to overcome these problems by calculating collisions between massive stars and computing the evolution of these merged objects did not result in very different conclusions (Suzuki et al., 2007c). Ide-

ally, one would like to perform a fully self-consistent simulation in which the stellar dynamics, the hydrodynamics of the stellar collisions and the further evolution of the collision products are taken into account self consistently. Such multiscale simulations, however, will have to await the development of the appropriate numerical methodology. The MUSE software environment may provide the necessary functionality for such simulations[1].

In this work we investigate the evolution of three massive stellar collision runaways with a detailed stellar evolution code. The template simulations we chose are three of the sequences published in Portegies Zwart et al. (2004). Each of the stars in the collision sequence are evolved up to the moment they collide using a stellar evolution code (described in §7.2.2) and each merger is resolved as described in §7.2.1. These hydrodynamical events result in a composition and structure of the collision product, of which the evolution is continued. We follow the evolution of the merger product until the evolution code fails to converge or until the onset of carbon burning, applying mass loss rates from the literature. We estimate the final mass of the merger and estimate the mass of the remnant of such a merger event. We also provide the chemical yields that result from such a merger sequence and compare them to the combined yields of a population of normal single stars. Finally we comment on the effect of the initial composition, especially the heavy element content Z (metallicity) on the structure of the merger remnant.

7.2 Methods

7.2.1 Stellar collisions

We use two different methods to model stellar collisions. The first assumes that the collision product is in hydrostatic and thermal equilibrium and mixed homogeneously. The second method uses the prescription of Gaburov et al. (2008) to model the structure of the remnant. In this case the collision product is not homogeneously mixed and it is not in thermal equilibrium (although it is still in hydrostatic equilibrium).

All collisions are treated as head-on collisions with vanishing velocity at infinity (*i.e.*, parabolic collisions). We ignore rotation in this work despite the fact that rotation can have a significant influence on the evolution of a massive star (Maeder & Meynet, 2000b).

Homogeneous mixing

In this approach, detailed models of the progenitor stars were merged and homogeneously mixed at each step of the sequence. We assume that the merger remnant is in hydrostatic and thermal equilibrium. The mass loss from the collision is estimated according to Gaburov et al. (2008).

[1] see `http://muse.li`.

In general, homogeneous mixing is not a good approximation for the structure of a merger remnant (Lombardi et al., 1996b; Gaburov et al., 2008; Glebbeek et al., 2008; Gaburov et al., 2008). However, Suzuki et al. (2007c) find that their collision products are almost completely mixed due to mixing processes during stellar evolution. Similarly, we find (§7.3.1) that the central convection zone in our merger remnants encompasses most ($\gtrsim 90\%$) of the stellar mass. Rotational mixing, which we have ignored, will result in even more extended mixing of the collision product, so homogeneous mixing is a reasonable approximation in this case.

Detailed merger models

Our detailed merger models were calculated using the Make Me A Massive Star (MMAMS) code by Gaburov et al. (2008). The code has a prescription for the mass lost from the collision that is based on the results of smooth particle hydrodynamics calculations. Heating due to the dissipation of the kinetic energy of the progenitor stars in shocks and tides is also taken into account. After the ejected mass has been removed and heating has been applied to the material from the parent stars the structure of the collision remnant is determined by searching for a configuration that is dynamically stable (*i.e.* satisfies the Ledoux stability criterion, Kippenhahn & Weigert, 1990). An algorithm for doing this was first developed by Lombardi et al. (2002b) for low-mass stars, for which it is sufficient to sort the mass shells in order of increasing entropy and then integrate the equation of hydrostatic equilibrium. This algorithm is referred to in the literature as *entropy sorting*. For massive stars where radiation pressure is important this does not necessarily produce a stable configuration and some mass shells need to be moved again after the equation of hydrostatic equilibrium has been integrated. This is repeated until a stable model is converged upon.

The output model is imported into the stellar evolution code using the method described in Glebbeek et al. (2008) and evolved until the time of the next collision.

Due to heating during the collision the merger product is not in thermal equilibrium. The excess of internal heat is radiated away during the contraction of the star to the main sequence. Because the stars were out of thermal equilibrium, we encountered more numerical problems when importing the stellar models than we did for the homogeneously mixed models, so that we could only follow one of the merger sequences until the seventh collision.

7.2.2 Stellar evolution

Our stellar evolution code is a version of the STARS code originally developed by Eggleton (1971b) and later updated by others (*e.g.* Pols et al., 1995). This version of the code uses the opacities from Iglesias & Rogers (1996) that

take into account enhancement of C and O, as described in Eldridge & Tout (2004) and Ferguson et al. (2005). The assumed heavy-element composition is scaled to solar abundances (Anders & Grevesse, 1989). Chemical mixing due to convection (Böhm-Vitense, 1958; Eggleton, 1972) and thermohaline mixing (Kippenhahn et al., 1980; Stancliffe et al., 2007) is taken into account. Note that thermohaline mixing is not important in these very massive stars, since most of the star is convective.

STARS uses an adaptive mesh in which the mesh points automatically redistribute themselves according to a mesh spacing function that places more meshpoints in regions of the star where a higher resolution is required. This allows us to calculate the structure of the star with a fairly small number of mesh points. For the models presented here we used 200 mesh points for the main sequence phase and 500 for the core helium-burning evolution. Because our stars form an extended low-density envelope (see §7.3.1) we have found it necessary to increase the number of mesh points in the outer layers compared to our standard stellar models.

We use a mass fraction of heavy elements $Z = 0.02$ for our standard runs. In order to study the effect of metallicity we have also recalculated one of our sequences with $Z = 0.001$. This affects the mass-loss rate and therefore the mass of the progenitors at each collision. We terminate the evolution at central carbon ignition and estimate the final remnant mass according to Belczynski et al. (2002).

7.2.3 Mass loss

Since our collision products become very massive and luminous, even exceeding the Humphreys-Davidson limit (a luminosity cutoff above which few stars are observed, Humphreys & Davidson, 1979), mass loss plays a key role in their evolution. Unfortunately, neither observations nor theoretical models of mass loss exists for the full range of masses and luminosities reached by our models. We have considered three possible mass-loss prescriptions: the empirical rate from de Jager et al. (1988) and theoretical rates from Vink et al. (2000, 2001) and Kudritzki (2002). None of these rates cover the range of parameters of our models well. The empirical de Jager rate has too few data points for luminosities above the Humphreys-Davidson limit. Their 20 point Chebyshev fit needs to be extended beyond $\log L/\mathrm{L}_\odot = 6.7$. The theoretical rate from Kudritzki needs to be extrapolated for $T_{\mathrm{eff}} < 40\,000\mathrm{K}$ while the models for the Vink rate are calculated for $\log L/\mathrm{L}_\odot < 6.25$ and $50\,000\mathrm{K} \lesssim T_{\mathrm{eff}} \lesssim 10\,000\mathrm{K}$.

We have made some trial calculations using these three mass loss prescriptions to decide which rate we should adopt for our calculations. The results of our trial calculations were qualitatively similar and independent of the mass-loss recipe used. For our quantitative analysis we have adopted the Vink et al. (2001) rate because of the three rates mentioned it best cov-

ers the range of effective temperatures for our models and only needs to be extrapolated in luminosity. By contrast, the Kudritzki (2002) rate needs to be extrapolated to lower effective temperatures, which is less reliable than extrapolating to higher luminosities because the presence of spectral lines that drive the wind depends sensitively on the temperature. In the region where the Kudritzki (2002) rate is valid it is very similar to our extrapolated Vink et al. (2001) rate. Note that our adopted mass-loss rate likely underestimates the true mass loss rate since our stars are much closer to their Eddington limit than the model calculations on which the Vink rate is based. We will return to this point in the discussion. The Vink rate is not applicable to red supergiants and predicts a mass loss rate that is too low for cool stars. For this reason we adopt the de Jager rate rather than the Vink rate at effective temperatures below 10 000K. Our models only reach this temperature for luminosities that are within the validity range of the de Jager rate.

All our models become helium-rich and evolve into Wolf-Rayet stars. We follow the criterion used by Eldridge & Vink (2006) to decide when our stars become Wolf-Rayet (WR) stars. Specifically, we start applying the mass-loss rate from Nugis & Lamers (2000) when the surface abundance of hydrogen drops below 40% by mass and $T_{\rm eff} > 10\,000$K. This happens *before* the star finishes core hydrogen burning (compare Langer et al., 2007; Yungelson et al., 2008). For our low metallicity run we used the metallicity scaling found by Vink & de Koter (2005) for the WR mass-loss rate. The Vink et al. (2001) rate already includes metallicity scaling.

7.2.4 Rotation

It has been shown that for off-axis collisions the angular momentum of the collision product can be so large that it cannot reach thermal equilibrium before losing a large fraction of its angular momentum (Lombardi et al., 1996b; Sills et al., 1997). We may therefore underestimate mass loss from the collision. The mechanism for this angular momentum loss is unclear but it has been suggested that magnetic fields can play a key role (Leonard & Livio, 1995; Sills et al., 2005). Rapid rotation can also enhance the mass-loss rate of a star, especially close to the Eddington limit (Maeder & Meynet, 2000a). This increases the uncertainty in the mass-loss rate.

Rotation also influences the star through various instabilities that can induce mixing (Endal & Sofia, 1976; Pinsonneault et al., 1989; Heger et al., 2000). This mixing is important because it can bring helium to the surface, affecting the opacity of the envelope and increasing the luminosity and effective temperature of the star. As mentioned above, rotational mixing is not expected to alter the outcome of our calculations very strongly because our collision products are close to being fully convective.

N	t	$M_{1,N\mathrm{body}}$	$M_{1,\mathrm{mix}}$	$M_{1,\mathrm{MMS}}$	M_2	M_{remnant}
1	0.22577	92.4	90.9	90.9	79.4	154.3
2	0.22782	171.8	154.3	152.8	85.3	217.1
3	0.23702	257.1	216.7	213.6	7.7	223.3
4	0.31217	264.8	219.8	215.3	77.8	274.4
5	0.40122	342.6	268.2	261.6	13.8	279.7
6	0.43480	356.4	277.2	268.0	71.9	327.1
7	0.43480	428.3	327.1	315.1	79.4	382.2
8	0.74123	507.7	348.2		30.1	371.8
9	0.83549	537.7	360.2		66.7	406.7
10	0.90575	604.5	397.3		1.2	398.5
11	1.29919	605.7	353.5		98.2	415.2
12	1.33450	703.9	411.0		24.2	430.8
13	1.42468	728.0	417.6		8.9	425.7
14	1.50261	736.9	409.0		2.2	411.2
15	1.60190	739.1	216.7		60.2	256.5
16	1.63186	799.4	221.0		9.2	228.9
17	1.68112	808.5	186.0		81.1	237.1
18	1.75684	889.6	177.3		40.9	205.5
19	1.90688	930.5	193.6		31.6	216.3
20	2.07245	961.9	129.9		2.6	132.2
21	2.59778	963.1	47.6		55.2	88.6
22	3.10786	1012.7	40.9		75.4[a]	110.1
	3.72835	1118.9	13.9			

[a] See text

Table 7.1: *Parameters and results of the first collision sequence studied in this paper. For each subsequent collision N we list the time of collision t (in Myr), the primary mass according to the N-body model $M_{1,N\mathrm{body}}$, the primary mass according to our models, assuming complete mixing during the collision $M_{1,\mathrm{mix}}$, the mass of the secondary M_2 and the mass of the remnant after the collision M_{merger} (all in solar masses). For comparison we also give the masses $M_{1,\mathrm{MMS}}$ for the MMAMS models that we were able to calculate. The final row gives the age at which our evolution calculations stopped and the mass of the collision product at the end of the evolution (assumed black hole mass).*

7.3 Results

The initial conditions and outcome of each of our merger sequences are listed in Tables 7.1, 7.2 and 7.3. The tables give the time of collision t, the secondary mass M_2 and the mass of the primary according to the different merger prescriptions. Sequence three was recalculated for $Z = 0.001$ and the results for this run are given in Table 7.4.

N	t	$M_{1,N\mathrm{body}}$	$M_{1,\mathrm{mix}}$	M_2	M_{merger}
1	0.72251	91.8	86.5	81.9	150.1
2	0.72252	173.7	150.1	80.2	206.7
3	0.88257	253.8	198.9	68.6	245.6
4	0.88522	322.5	245.4	72.9	294.5
5	0.95998	395.4	287.7	1.8	289.4
6	1.41050	397.1	250.0	95.8	309.6
7	1.50639	492.9	298.4	86.1	352.3
8	1.97200	578.8	282.1	97.6	338.2
9	2.22324	676.2	79.8	75.2	130.4
10	2.22325	751.5	130.2	55.4	166.3
11	2.45320	806.7	83.9	23.5	100.4
12	2.68305	829.8	66.7	28.4	86.8
13	2.74781	858.0	78.8	1.0	79.8
14	3.08766	857.3	53.5	82.6	105.2
15	3.19983	939.2	46.1	56.3	86.3
16	3.27682	995.0	64.8	41.6	93.6
	4.51074	1036.6	10.1		

Table 7.2: *As Table 7.1 for collision sequence 2*

N	t	$M_{1,N\mathrm{body}}$	$M_{1,\mathrm{mix}}$	M_2	M_{merger}
1	0.53120	77.8	75.3	70.7	131.5
2	0.57294	148.5	130.7	82.8	191.3
3	0.65612	231.3	188.1	58.5	228.6
4	0.89154	289.8	215.4	96.6	279.9
5	0.89155	386.4	279.9	78.5	332.5
6	1.02208	464.9	318.1	1.5	319.5
7	1.31086	466.4	289.3	56.3	327.9
8	1.50575	522.6	305.7	48.9	340.1
9	2.05327	571.3	164.0	72.7	209.2
10	2.27966	643.8	73.1	2.0	74.8
11	2.60213	645.0	35.1	3.5	37.7
12	3.12235	642.8	19.8	49.3	60.7
	4.59400	692.1	9.7		

Table 7.3: *As Table 7.1 for collision sequence 3*

The evolution track in the Hertzsprung-Russell diagram for the first merger sequence (Table 7.1) is shown in Figure 7.1. The two other sequences are similar. The location of the ZAMS (up to 200 $\mathrm{M}_\odot$) is indicated with a dashed line and every 30 000yr is marked with •. The repeated collisions

N	t	$M_{1,N\mathrm{body}}$	$M_{1,\mathrm{mix}}$	M_2	M_{merger}
1	0.53120	77.8	77.7	70.7	135.4
2	0.57294	148.5	135.4	82.8	198.3
3	0.65612	231.3	198.1	58.5	239.6
4	0.89154	289.8	239.1	96.6	308.5
5	0.89155	386.4	308.5	78.5	364.2
6	1.02208	464.9	363.5	1.5	364.9
7	1.31086	466.4	363.4	56.3	404.7
8	1.50575	522.6	403.4	48.9	440.2
9	2.05327	571.3	434.9	72.7	487.5
10	2.27966	643.8	390.1	2.0	392.0
11	2.60213	645.0	260.1	3.5	263.3
	2.83153	648.5	171.9[b]		

[b] Mass and time at the moment the evolution failed to converge, rather than the onset of carbon burning.

Table 7.4: *As Table 7.3 but for $Z = 0.001$. Note that the merger sequence was terminated earlier than for $Z = 0.02$ and that the merger remnant did not finish its evolution before the evolution code broke down.*

N	t	$M_{1,N\mathrm{body}}$	$M_{1,\mathrm{mix}}$	M_2	M_{merger}
1	0.88048	66.6	63.6	65.2	113.4
2	1.08887	131.8	110.4	16.4	114.1
	3.10786	106.2	75.4		

Table 7.5: *Times t and secondary masses m_2 for the sub merger sequence leading to the secondary of collision 22 in the merger sequence in Table 7.1.*

drive the collision product to high luminosities, exceeding the Humphreys-Davidson limit, but the collision product never moves far from the extension of the ZAMS, instead evolving nearly vertically in the HR diagram (similar to the evolution tracks for homogeneously evolving stars, Yoon & Langer, 2005). For reference, the locations of the Pistol Star and η Carinae are also shown. The location of η Car is based on Hillier et al. (2001), with the spread in effective temperature due to the spread in their radius estimates. The luminosity is based on the infrared flux. The location of the Pistol Star is based on the low luminosity solution of Figer et al. (1998b). We see that the merger remnant is always hotter than either of these two stars, except when it becomes a red supergiant (the red loop in Figure 7.1), at which time it is less luminous. During the merger sequence the luminosity can exceed the luminosity of these stars. On the other hand, η Carinae and the Pistol Star are both obscured by optically thick outflows, which means that comparing with the effective temperature of our model can be misleading

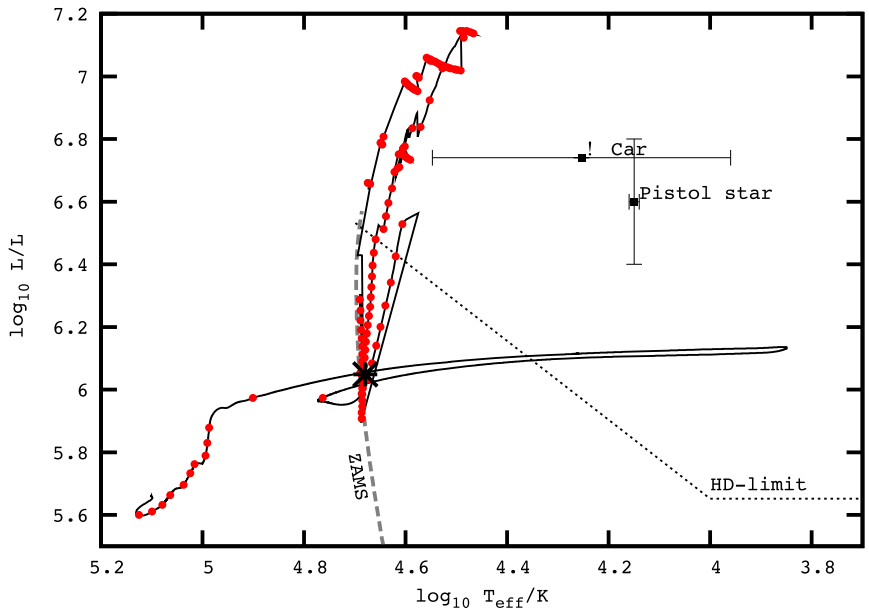

Figure 7.1: *Evolution track of the merger from sequence 1 in the Hertzsprung-Russell diagram. The starting point is indicated by ∗ and points are plotted on the evolution track after each* 30 000 yr. *The dotted line indicates the Humphreys-Davidson limit. For reference, the theoretical ZAMS (running up to 200* $M_\odot$*) and the locations of η Carinae and the Pistol Star are also plotted.*

because we do not model such an optically thick wind. The location of the collision product above the Humphreys-Davidson limit suggests that it is a luminous blue variable (LBV) star, so that in reality its position in the HRD is likely to be variable.

The high luminosity increases the mass-loss rate, leading to a competition between mass loss due to stellar winds and mass increase due to collisions. The time evolution of the mass of the mergers is shown in Figure 7.2. The dashed lines give the mass that was predicted in the N-body simulation while the solid lines show our fully mixed models for $Z = 0.02$. The two agree well for the first few collisions, but mass loss due to stellar wind prevents the mass from exceeding $500\,M_\odot$. The surface of the merger remnants becomes helium rich and after 1.5–2 Myr turns the star into a Wolf-Rayet star. The strong WR mass-loss rate (up to $3.6 \cdot 10^{-3}\,M_\odot\,\mathrm{yr}^{-1}$ when the collision product first becomes a WR star) brings the mass down very quickly, to $\sim 100\,M_\odot$ after the final collision and 10–14 $M_\odot$ at the time of carbon ignition.

In Figure 7.3 we follow the evolution of the radius. Our collision products have substantially larger radii (up to a factor three, note the logarithmic scale) than predicted by the N-body code, despite the smaller mass. This

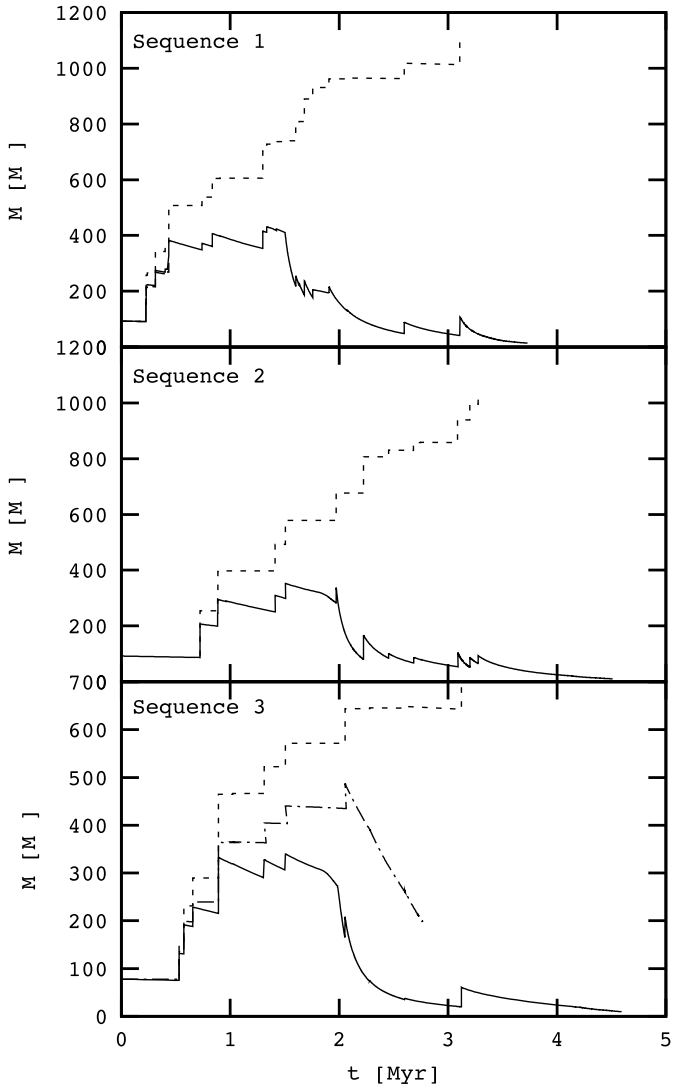

Figure 7.2: *The mass of the merger product as a function of time for the three merger sequences listed in Tables 7.1–7.3. The solid line is the mass found from the detailed models assuming homogeneous mixing, the dashed line is the mass predicted from the N-body calculation. The dash-dotted line in the bottom panel is the mass of the* $Z = 0.001$ *run.*

is due to a peculiarity in the structure of the collision product, which will be discussed in detail in §7.3.1. When the collision product becomes a WR star, the radius decreases substantially and the collision product can be up to an order of magnitude smaller than was assumed in the N-body calculation. After core hydrogen exhaustion the collision product still has a thin hydrogen-poor ($X \approx 4\%$) envelope. Expansion of this envelope is

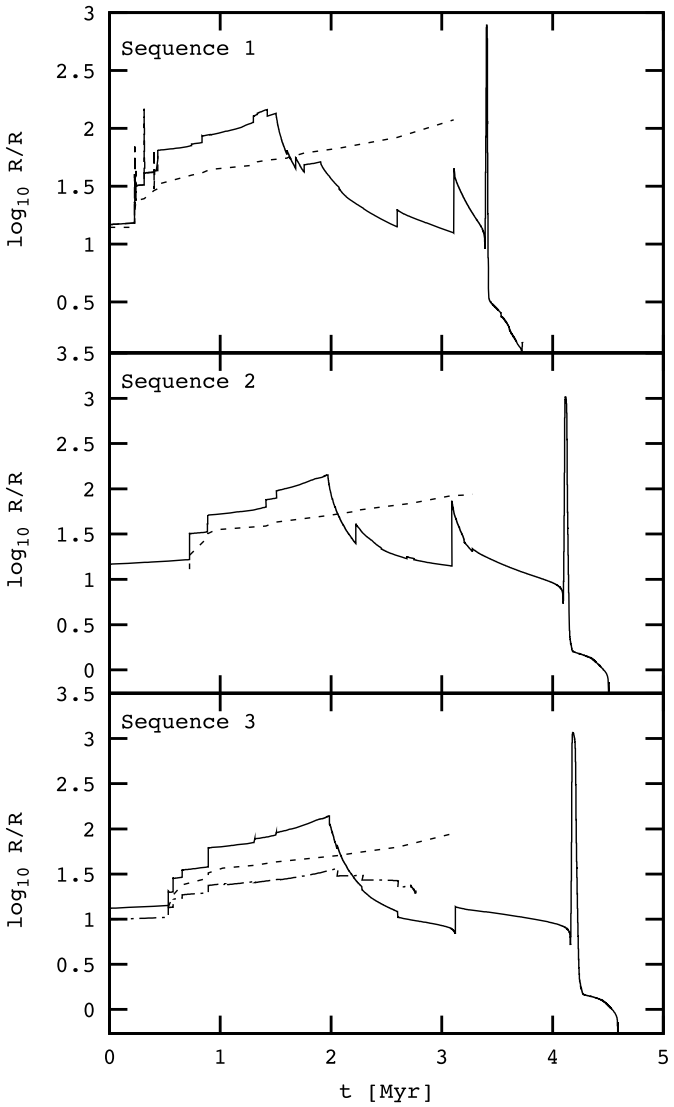

Figure 7.3: *The radius of the merger remnant of the three sequences against time. The solid line is the prediction from our homogeneous models while the dashed line is the radius from the N-body code. The long dashed line in the top panel is the radius from the MMAMS model, which shows spikes at each collision because the merger remnant is out of thermal equilibrium immediately after the merger. The dash-dotted line in the bottom panel is the radius of the* $Z = 0.001$ *run.*

responsible for turning the star into a red supergiant and causes the spike in the radius at 3.5 Myr (first sequence) and 4.1 Myr (second and third sequence). During the red supergiant phase the collision product is again above the Humphreys-Davidson limit, but this phase is very short, lasting

$17 \cdot 10^3$yr ($< 1\%$ of the lifetime of the star).

We have also plotted the mass and radius from the MMAMS models that we were able to calculate. In the upper panel of Figure 7.2 the MMAMS model is indistinguishable from the homogeneous model. After the collision the merger remnant is out of thermal equilibrium and is inflated. The increase in radius at each collision can be seen in the upper panel of Figure 7.3. Once the collision product reaches thermal equilibrium (after $\sim 10^4$ yr) the radius closely follows the radius of the homogenised model, indicating that the homogenised model is indeed a reasonable approximation of the structure of the merger remnant. Because the radius is larger while the collision product is out of thermal equilibrium it is more likely to interact or collide with other stars at this time, but since we do not take feedback on the dynamics into account this effect is not important for our present considerations.

The collision sequences mostly involve main-sequence stars but a few of the listed collisions are special. Collision 22 of the first sequence involves the remnants of two collision runaways. The star that has undergone the longest sequence of collisions (the "primary") is an early type Wolf-Rayet star at this point with a surface hydrogen abundance of 0.24 and a mass of $41\mathrm{M}_\odot$. However, it is still undergoing core hydrogen burning. The star that has undergone the shortest merger sequence (the "secondary", see Table 7.5) is a core helium burning star of $75\mathrm{M}_\odot$ that has not yet become a Wolf-Rayet star (although it is close to fulfilling our criteria) and has a surface hydrogen abundance of 0.44. In our homogeneous mixing treatment the result is a collision product that has been enhanced in carbon (see the surface abundance plot in Figure 7.5), which is converted into nitrogen through CNO processing. In a more detailed treatment of the merger process we expect the dense helium core of the secondary to sink to the centre of the collision product so that the merger remnant would have a hydrogen depleted core.

A similar situation occurs for collision 14 from the second sequence, for which the secondary has also become a core helium-burning star at the time of collision.

7.3.1 Structure and size of the merger remnants

During dynamical interactions in a dense cluster, the size of the merger remnant is one of the parameters that determines the probability of subsequent collisions. As mentioned, the large radius of the $Z = 0.02$ models during the first 1.5–2 Myr in Figure 7.3 is caused by a peculiarity of the stellar structure.

The merger remnants become very massive and are almost fully convective. The lower panel in Figure 7.4 shows the location of convection zones against the enclosed mass, the upper panel shows the same information as a function of the radius. The central convection zone contains about 90%

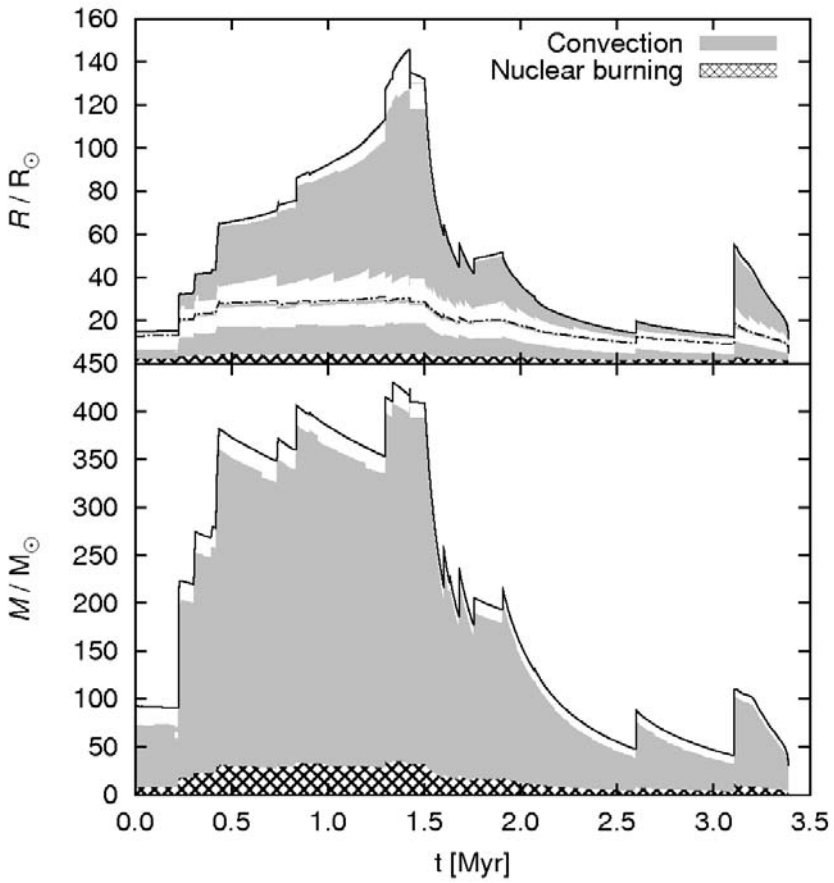

Figure 7.4: *Kippenhahn diagram showing the evolution of the collision product of the first merger sequence. The plot shows convection zones against the radius (upper panel) and against mass coordinate (lower panel) as a function of time. In the upper panel the radius containing a fraction* $1 - 10^{-5}$ *of the stellar mass is indicated with a dash-dotted line. The convective core encompasses 90% of the mass but a much smaller fraction of the radius (at most* $20\,\mathrm{R}_\odot$*). Mass loss between collisions exposes material from the convective core.*

by mass of the merger remnant. As can be seen from the figure, mass loss between the collisions can reveal material from the central convection zone at the stellar surface (for instance, the mass of the star at 1.3 Myr is lower than the mass of the convective core at 0.8 Myr).

The outer 10% by mass of the merger remnant is radiative, but the upper panel of Figure 7.4 shows two convection zones in this region which correspond to different peaks in the opacity of the stellar material. An

extended convective layer that corresponds to the "Fe bump" is located at large radii. The Fe bump is an increase in opacity around $\log T \approx 5.3$ which was found after introducing the treatment of spin-orbit splitting of iron and nickel into the computation of the opacity tables (Rogers & Iglesias, 1992; Seaton et al., 1994). Deeper down a thin convective layer can be seen, caused by the "deep Fe bump", occurring around $\log T \approx 6.3$.

Together, these convection zones are very extended in radius but contain almost no mass. It is especially the convection zone corresponding to the Fe-bump which expands even more while the star evolves. When the star reaches its maximum radius of about 150 $R_\odot$ after 1.4 Myr, this convection zone extends over 90 $R_\odot$, while it contains only about $10^{-4}\,M_\odot$. At this moment the star consists of a core of less than 30 $R_\odot$ in size containing almost all of the mass surrounded by an extended "halo" reaching from 30 to 150 $R_\odot$. This halo has an almost constant temperature and density of $10^{-10}\,\mathrm{g\,cm^{-3}}$. This is indicated in Figure 7.4, which shows the radius outside which a fraction 10^{-5} of the stellar mass is located.

This "core-halo" structure has been found before in models of massive stars, for example by Ishii et al. (1999) for hydrogen-rich stars and by Petrovic et al. (2006) for helium stars. Petrovic et al. (2006) note that to provide the high mass-loss rate from the surface a large outward velocity is needed in the outer layers where the density is low. In their models the necessary velocity is larger than the local sound speed by an order of magnitude. This means that the halo cannot be modelled realistically under the assumption of hydrostatic equilibrium and may not be stable. They find that with a more detailed treatment the halo disappears as a result of the high mass-loss rate. Because our merger remnants have a much larger radius the outflow velocity in the halo is about 2–3 orders of magnitude smaller than the sound speed, which suggests that the halo structure is stable in this case. The halo disappears when the merger remnants become Wolf-Rayet stars and the mass-loss rate increases.

7.3.2 Final remnant masses

For each of the three merger sequences the collision product is close to core hydrogen exhaustion when the merger sequence ends. After the end of the main sequence hydrogen continues to burn in a shell very close to the surface. The hydrogen envelope expands, driving the star into a red loop in the HRD. Mass loss from the surface gradually removes the hydrogen envelope, reducing the efficiency of the hydrogen burning shell. When the hydrogen shell is extinguished the star returns to the blue part of the Hertzsprung-Russell diagram. The remaining hydrogen envelope is lost and the star becomes a massive ($\sim 20 - 30 M_\odot$) helium star. By the end of core helium-burning the mass has gone down to $10 - 14\,M_\odot$, 80% of which is taken up by the C/O core. The expected outcome of the evolution for such stars is a

	Sequence 1	Sequence 1		
	Single	Collision	Wind	
ΔM	647.5	228.6	695.8	95.4
H	0.4806	0.5648	0.4006	0.0899
He	0.4965	0.4000	0.5794	0.8308
C	0.0040	0.0012	0.0003	0.0306
N	0.0092	0.0166	0.0132	0.0294
O	0.0040	0.0013	0.0010	0.0060

	Sequence 2			Sequence 3		
	Collision	Wind	Remnant	Collision	Wind	Remnant
ΔM	191.8	549.9	83.5	142.3	456.6	102.0
H	0.5599	0.3489	0.1944	0.5521	0.3361	0.2025
He	0.4093	0.6311	0.7637	0.4305	0.6439	0.7553
C	0.0090	0.0003	0.0133	0.0004	0.0003	0.0184
N	0.0117	0.0133	0.0128	0.0105	0.0134	0.0123
O	0.0044	0.0009	0.0081	0.0013	0.0008	0.0050

Table 7.6: *Ejected mass and composition for the three computed merger sequences compared to a population of single stars. The first row lists the total mass ΔM (in solar units) lost through each of the three listed channels, the remaining rows give the abundances (by mass) of H, He, C, N and O. For each sequence the first column lists the ejecta from the collision, the second column lists the integrated values for the stellar wind during the merger sequence and the third column lists the values for the evolution of the merger remnant after the merger sequence has ended. The single star yields correspond to the stars involved in the first merger sequence.*

complete collapse to a black hole (Belczynski et al., 2002).

In each of these sequences $600 - 900\,\mathrm{M}_\odot$ is lost to the interstellar medium. Most of this material is lost due to stellar wind between collisions (see Table 7.6) rather than in the ejecta of each collision.

7.3.3 Surface abundances and chemical yields

In the course of its evolution the surface of the merger remnant gradually becomes helium rich, as can be seen in the top panel of Figure 7.5. The CNO abundances (shown in the bottom panel of Figure 7.5) change strongly at the first collision and then stay mostly constant up to $t \approx 3\,\mathrm{Myr}$.

The abundances change most strongly during collisions. This is because the merger remnant is fully mixed at this stage. The abundances also change in between the collisions, as mass loss strips away the surface layers and reveals the deeper layers, but the change is not visible on the scale of the plots until the merger remnant becomes a Wolf-Rayet star. In sequences 1 and 2 the merger remnant undergoes a collision with a core helium-burning

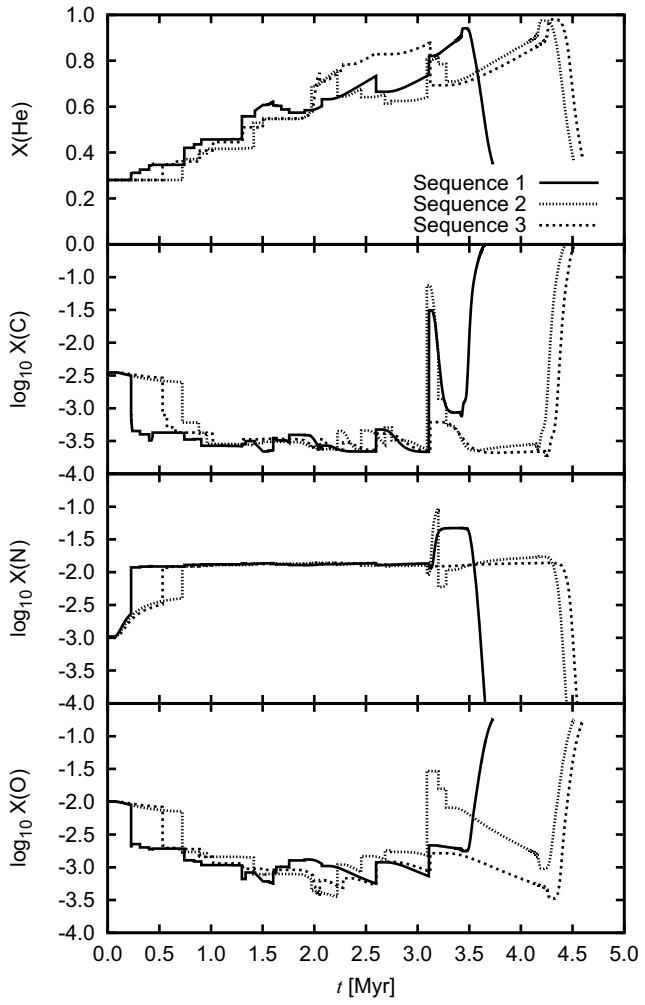

Figure 7.5: *Surface He, C, N and O abundances (by mass fraction) for as a function of time (in Myr) for the three $Z = 0.02$ sequences.*

star at 3Myr. This results in a strong increase in the carbon abundance (and oxygen, for sequence 2) and a decrease in the nitrogen abundance (through dilution). CNO cycling then converts the carbon into nitrogen, producing a nitrogen-rich WR star. However, our assumption of complete mixing is unlikely to be valid for collisions with core helium-burning stars. More likely, most of the carbon and oxygen would remain in the core of the collision product and such a strong increase in surface C and N probably

does not occur.

As the collision product continues to evolve after the end of the merger sequence, the surface helium abundance increases until the hydrogen envelope has been lost and the surface is nearly pure helium. The stellar wind continues to expose deeper layers of the star, eventually revealing at the surface the ashes of helium burning. At this point, the surface nitrogen and helium abundance decrease while the carbon and oxygen abundances increase strongly. At the end of the evolution, carbon is the most abundant element on the surface.

The expulsion of gas from the cluster is usually attributed to supernova explosions, which are expected to start after about 3 Myr. The merger remnant loses most of its mass before this time. Table 7.6 gives the composition of the material lost from the merger remnant as well as the amount of material lost, split into three categories: ejecta from the collisions, mass loss due to stellar wind during the merger sequence and mass loss from the collision product after the end of the merger sequence. Most of the material is ejected in the form of a stellar wind between collisions, followed by the material that is lost during the collisions. The material that is lost by the collision product after the end of the merger sequence is significantly more helium rich than the material that was lost before. This simply reflects the increased surface helium abundance of the collision product. The material lost from the collisions is less helium rich than the material that is lost in the wind. This is partially due to the increase in the surface helium abundance between collisions (Figure 7.5) and partially due to the fact that the estimated mass loss from the collision is larger for more equal masses and becomes smaller when the mass ratio is more extreme, which is the case for later collisions when the collision product is both massive and helium rich.

If we compare the yields of the first sequence to the yields that would have been obtained if the stars involved in the merger had been allowed to evolve on their own (column 2 in Table 7.6) we first note that the single stars eject much less material than the merger sequence. This is because the merger sequence produces one 13.9 $M_\odot$ black hole, while the single stars above 30 $M_\odot$ all produce black holes of 8–24 $M_\odot$. The ejected material is also less helium rich than the material that is lost from the merger remnant: the single star models lose 321 $M_\odot$ of helium and 311 $M_\odot$ of hydrogen (He/H $\approx$ 1), while the merger product loses 574 $M_\odot$ of helium and 416 $M_\odot$ of hydrogen (He/H $\approx$ 1.4). This is directly related to the large size of the convective core: for the merger remnant, 90% of the material has undergone nuclear processing in the core, which is a much larger fraction than for the population of single stars.

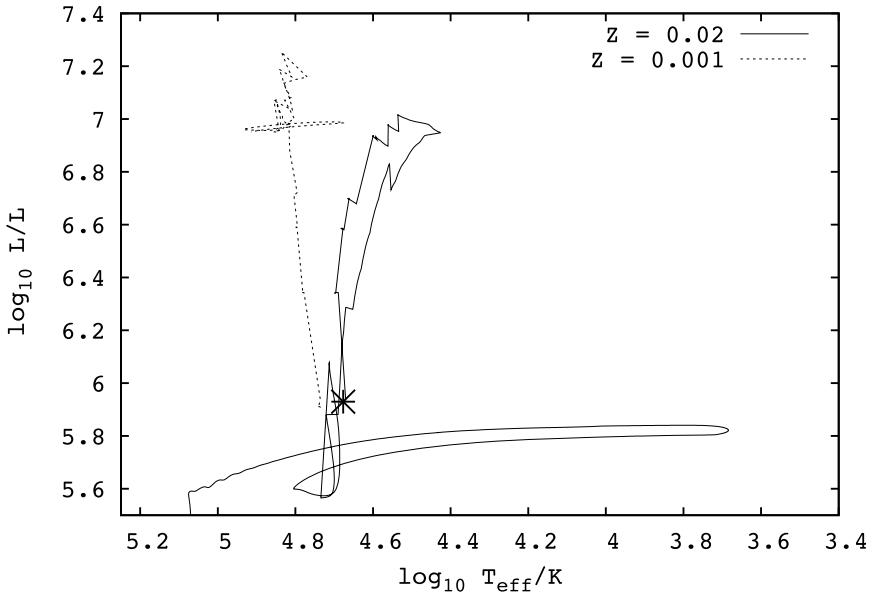

Figure 7.6: *Evolution track of the merger remnant of sequence 3 for $Z = 0.02$ (solid line) and $Z = 0.001$ (dashed line). Note that the $Z = 0.001$ track remains much brighter than the $Z = 0.02$ track.*

7.3.4 Metallicity effects

Because mass-loss rates are lower at low metallicity we have recalculated sequence 3 for $Z = 0.001$. At this metallicity the mass-loss rates are about 13 times lower than for $Z = 0.02$, which means that the remnant can become more massive.

The mass of the remnant after the last collision in the sequence is $263\mathrm{M}_\odot$. We followed the evolution of the merger product through core helium burning until the core helium abundance has decreased to $Y_\mathrm{c} \approx 0.63$ (about one third of the core helium-burning lifetime), at which time the mass is $172\,\mathrm{M}_\odot$. Numerical problems prevented us from evolving this model further until carbon ignition. We extrapolated the mass loss as a linear function of the central helium abundance (rather than time) to the moment of helium exhaustion, which was found to give a good estimate of the final mass for $Z = 0.02$. Based on this extrapolation we expect the final mass to be $\sim 120\mathrm{M}_\odot$ by the time of carbon ignition. The expected fate of this merger remnant is a pair-creation supernova (Langer et al., 2007; Portegies Zwart & van den Heuvel, 2007).

Because the opacity bump that gives rise to the core-halo structure is associated with iron, the core-halo structure does not appear at low metallicity and the collision product remains more compact. This is why in the bottom panel of Figure 7.3 the radius of the $Z = 0.001$ model (dash-dotted

line) is smaller than the radius of the $Z = 0.02$ model until 2 Myr, when the latter becomes a WR star. The radius is always smaller than the radius assumed in the N-body calculations.

The lower mass-loss rate makes it easier to build up more massive remnants, but the smaller radius reduces the probability of a collision and may prevent the occurrence of a runaway merger. The thermal timescale is also shorter at low metallicity, meaning that the star will reach thermal equilibrium faster after the collision. An additional complication is that the lifetime of the stars is reduced at lower metallicity (because of their larger mass) so that there is less time to form the merger sequence. Fully self-consistent dynamical models (in which the stellar evolution, stellar collisions and stellar dynamics are all treated consistently) are necessary to determine which of these effects dominates in practice.

7.4 Discussion and conclusions

We have found that the end result of a runaway merger at solar metallicity is a $\sim 100\mathrm{M}_\odot$ WR star after the final collision that produces a $\sim 10\mathrm{M}_\odot$ black hole. Most of the mass is lost in the form of a stellar wind enriched in N and He. At lower metallicity the mass-loss rates are reduced and the remnant mass can be larger ($\sim 260\,\mathrm{M}_\odot$), possibly leading to a pair-creation supernova. In none of the cases we studied an intermediate-mass black hole is formed.

The material that is lost from the collision remnant is helium rich and shows the signature of CNO processing (N enhancement, C depletion). Because the merger remnant loses most of its mass in the first 3 Myr, the timescale on which we expect the first supernovae to go off, the primordial gas may not yet have been expelled from the cluster. In this case the material that is lost from the merger remnant can be retained in the cluster and could be accreted onto other stars or used in further star formation. This offers the possibility of finding a chemical signature in clusters observed today where a merger sequence occurred in the past. In order to do this we require more detailed nucleosynthesis than the models described in this paper provide. The amount of ejected material is probably not enough to account for a second generation of helium-rich stars as is found in some globular clusters, since such a helium-rich population generally seems to comprise about 15–20% of the stars in the cluster (Pumo et al., 2008), which is larger than the fraction of mass mass lost from the merger remnant compared to the total cluster mass.

The main uncertainty in our models is the adopted mass-loss rate. We have used established mass-loss prescriptions from the literature. Our adopted Vink et al. (2001) rate is derived for stars that are further away from their Eddington luminosity than our collision products and is likely to be an un-

derestimate of the true mass-loss rate for our stars.

When the surface hydrogen abundance $X_{\rm s} < 0.4$ we apply WR mass loss rates. This transition is somewhat arbitrary and ideally we would use a single mass loss recipe that predicts the mass-loss rate as a function of the local luminosity, temperature, effective gravity and composition. No such recipe is available in the literature at this time.

The mass-loss rate can become very high during the WR phase due to our extrapolation of the empirical rate to higher luminosity than for which it was derived. We have made sure that the power used to drive the wind is always less than that provided by the star's luminosity (Owocki et al., 2004). When the collision products first become WR stars, the mass-loss rate is still very high. In part this is due to the sudden transition to to WR mass loss rates when $X_{\rm s}$ drops below 0.4. We expect that if the transition is made more smoothly the mass-loss rate would increase earlier and avoid the high peak value found in our current models. This again stresses the need for a unified single mass loss prescription.

Our collision products have luminosities close to their Eddington luminosity and for a substantial amount of time exceed the Humphreys-Davidson limit. Stars close to this limit become luminous blue variables which can lose a large amount of mass in outbursts. A model that describes mass loss from stars that exceed their Eddington luminosity is the so-called porosity model (Owocki et al., 2004; Owocki & van Marle, 2008). Our models come close, but do not exceed their Eddington luminosity. We have made one trial run with the mass-loss rate artificially enhanced by a factor of 50 and found that the star is very quickly stripped of its mass.

We have ignored rotation in this work. Rotational mixing is expected to be unimportant because our models are almost fully convective. Rapid rotation is also expected to enhance the mass-loss rate from stars, especially close to the Eddington limit. This enhanced mass loss is compounded by the need to lose angular momentum from the collision product before it can reach thermal equilibrium. In effect this increases the uncertainty in the already uncertain mass loss rate.

The radius of our detailed evolution models is different from the radius that was used to detect collisions in the N-body run. This demonstrates that it is important to perform fully self-consistent simulations of collision runaways. Calculations at lower Z are especially interesting since remnant masses can be higher due to a reduced stellar wind, but on the other hand collisions are less likely because the stars are more compact. Calculations like those by Belkus et al. (2007) in which the stellar evolution is treated with an analytic recipe, are an important step in this direction.